

[Open Peer Review on Qeios](#)

Vimentin Regulates Collagen Remodeling Through Interaction with Myosin 10

Zofia Ostrowska-Podhorodecka¹, Isabel Ding¹, Sevil Abbasi¹, Masoud Norouzi¹, Aiman Ali¹, Pamma D. Arora¹, Timothy H.F. Wong¹, Marco Magalhaes¹, Christopher A. McCulloch¹

¹ University of Toronto

Funding: This study was supported by a Canadian Institutes of Health Research (CIHR) grant (MOP-503020) and by a Canada Research Chair (CAM).

Potential competing interests: The authors declare no conflicts of interest.

Abstract

Vimentin (Vim) marks epithelial-mesenchymal transition and increased Vim expression is associated with tumor progression and poor prognosis in colorectal cancer (CRC). Unconventional myosin 10 (Myo10) is an actin-based motor protein whose expression correlates with cancer metastasis, but the interactions of Myo10 with Vim in migrating cells are not defined. Sections of human invasive CRC exhibited prominent colocalization of Myo10 with Vim in cell extensions localized to the subjacent matrix, suggesting an association with local invasion. In mouse fibroblasts, Myo10 co-precipitated with Vim. Surface plasmon resonance showed high affinity binding of Myo10 to Vim (Kd 57 nM). By STED microscopy and FRET analysis, we found that Myo10 interacted with Vim at the termini of cell extensions. Deletion of Vim promoted accumulation of Myo10 at the cell periphery and reduced Myo10 at the tips of extensions. Drug-mediated disassembly of Vim filaments promoted Myo10 retraction from cell extensions into the cell body. FRAP showed that the mobility of Myo10 along cell extensions was impacted by Vim. Myo10 and Vim were required for pericellular collagen degradation by MT1-MMP. Vim deletion reduced the transit of MT1-MMP to the tips of cell extensions and down-regulated collagenolytic activity, which mediated cell invasion of the matrix. Deletion of Vim and Myo10 was associated with reduced collagen fiber alignment and tractional remodeling of the collagen matrix. CRC SW480 cells exhibited similar changes in Myo10 mobility and collagen remodeling after Vim knockdown, similar to mEFs, suggesting that Vim-Myo10 interactions are an important feature of motile cells. Collectively these data indicate that Vim binding to Myo10 promotes collagen remodeling and the generation of cell extensions required for cell migration through soft connective tissues.

Zofia Ostrowska-Podhorodecka^{a*}, Isabel Ding^a, Sevil Abbas^a, Masoud Norouzi^a, Aiman Ali^c, Pamma D. Arora^a, Timothy H.F. Wong^a, Marco Magalhaes^{bcd} and Christopher A. McCulloch^a

^a Faculty of Dentistry, University of Toronto, Toronto, ON M5G 1G6, Canada

^b Cancer Invasion and Metastasis Laboratory, Faculty of Dentistry, University of Toronto, Toronto, Ontario, Canada

^c Oral Pathology and Oral Medicine, Faculty of Dentistry, University of Toronto, Toronto, Ontario, Canada

^d Dental and Maxillofacial Sciences Department, Sunnybrook Health Sciences Centre, Toronto, Ontario, Canada

***Correspondence:**

Z. Ostrowska-Podhorodecka,
Room 461, 124 Edward Street, Toronto, ON Canada M5G 1G6
e-mail: zofia.ostrowska.podhorodecka@utoronto.ca
Telephone: 437-772-4388

Key Words: vimentin, myosin-10, MT1-MMP, collagen remodeling

Abbreviations:

epithelial-mesenchymal transition, EMT
extracellular matrix, ECM
vimentin, Vim
unconventional myosin X, Myo10
membrane-type 1 matrix metalloproteinase, MT1-MMP
collagen, Col

Introduction

Cell motility and migration are essential for myriad physiological and pathological processes including wound healing, tissue regeneration, and tumor metastasis. The importance of cell migration in metastatic processes and human health is underlined for example by the contribution of invasive colorectal carcinoma to cancer-related deaths worldwide. In developing nations, there has been a progressive rise in mortality rates as a result of poorly controlled colorectal cancer ([Rawla et al., 2019](#)). In colon cancer, epithelial-mesenchymal transition (EMT) is associated with invasion and metastasis ([Brabletz et al., 2005](#)). EMT manifests as loss of the epithelial phenotype and the acquisition of mesenchymal cell characteristics, which has been modeled by SW480 cells, highly motile elongated cells with prominent cell extensions or in the non-motile phenotype that are rounded ([Lam et al., 2018](#)). SW480 cells are widely used for study of cancer growth and progression ([Delaine-Smith et al., 2019](#)).

Transition through EMT involves the activation of new transcriptional programs, which initiate the disassembly of intercellular junctions and detachment of epithelial cells from the underlying basement membrane ([De Craene and Berx, 2013](#), [Nieto, 2009](#), [Thiery et al., 2009](#)). Cells that undergo EMT often exhibit enhanced migration, which is associated with reduced cytokeratin expression and increased expression of proteins associated with mesenchymal cell lineages including vimentin (Vim) and type I collagen (Col) ([Kaimori et al., 2007](#), [Lamouille et al., 2014](#), [Shibue and Weinberg, 2017](#)). Cell migration relies on the coordinated regulation of cytoskeletal components including the Vim filament network, which participates in the formation of polarized cell protrusions ([Ding et al., 2020](#)) and the assembly of intercellular junctions ([Sanghvi-Shah and Weber, 2017](#)). Vim, a class III intermediate filament protein, is involved in the transfer of mechanical force from cell-matrix adhesions to the cell interior ([Gregor et al., 2014](#), [Tsuruta and Jones, 2003](#)). Increased Vim expression is one of the hallmarks of EMT in epithelial cells and is associated with enhanced migration over the

underlying extracellular matrix (ECM) and the progression and metastatic potential of several types of cancers (Terriac et al., 2017, Danielsson et al., 2018, Strouhalova et al., 2020). Accordingly, there has been considerable interest in the role of Vim in cancer cell migration through soft connective tissues. The relatively high abundance of Vim in mesenchymal cells and its underlying dynamic structure (e.g., conversion of protofilaments to unit-length filaments to filaments), contribute to the regulation of cell adhesion strength and 2D cell migration (Ding et al., 2020, Helfand et al., 2011, Ostrowska-Podhorodecka et al., 2021). Further, Vim is an integral part of the adhesion complex that generates contractile forces for cell migration but that also confers resistance to deformation of migrating cells (Messica et al., 2017, Petrie et al., 2014). Despite intensive investigation, the mechanism by which Vim regulates Col remodeling in mesenchymal or cancer cells, especially in the early stages of cell adhesion and spreading, is not well defined.

Cell migration through soft connective tissues involves tractional remodeling and proteolysis of the extracellular matrix (ECM). Focal proteolysis of ECM is one of the first steps in matrix invasion by cancer cells, which is mediated in part by membrane-type 1 matrix metalloproteinase (MT1-MMP), a membrane-anchored proteinase expressed by invasive cancer cells (Watanabe et al., 2013). Vim is required for efficient surface translocation of MT1-MMP, which facilitates cell migration (Kwak et al., 2012) and penetration of the collagen matrix (Zhang et al., 2012). MT1-MMP promotes tumor invasion by functioning as a pericellular collagenase that activates pro-MMP2 and is directly linked to tumor progression (Aplin et al., 2009). MT1-MMP colocalizes with Myo10 at cell extension sites (Sun et al., 2019). Notably, silencing of Myo10 expression in human breast adenocarcinoma cells reduces the activation of MT1-MMP, suggesting a central role for Myo10 in controlling ECM degradation (Cao et al., 2014, Sun et al., 2019).

Myosin 10 (Myo10), an unconventional myosin, is an actin-based motor protein that is concentrated at the leading edge of cells and in early stages of cell spreading, Myo10 localizes at the tips of filopodia on the leading edge of cells, where it undergoes repetitive forward and rearward movements. When overexpressed, Myo10 promotes increased numbers and length of filopodia and their conversion to long cell extensions (Berg and Cheney, 2002, Hirano et al., 2011, Zhang et al., 2004). Myo10 promotes filopodia formation by delivering specific cargos to the cell periphery (Tokuo et al., 2007). In endothelial cells, Myo10 mediates the transport of VE-cadherin to cell edges and filopodia to support the contacts between cells (Almagro et al., 2010). Myo10 promotes cell attachment to the ECM via its interaction and trafficking of integrin to the tips of cell extensions, where Myo10 tethers integrin receptors, which is followed by talin-dependent integrin activation (Miihkinen et al., 2021).

We previously demonstrated how Vim expression regulates integrin-dependent cell adhesion and migration (Ostrowska-Podhorodecka et al., 2021). Currently the functional relationship between, and the regulation of, Myo10 and Vim, are not well-understood. Here we show a direct interaction between Myo10 and Vim in cell extensions, which contributes to Col remodeling and MT1-MMP-dependent collagenolytic activity in the context of cell migration through soft connective tissues and cancer progression.

Results

1. *Vimentin colocalizes with myosin 10 in invasive colorectal cancer*

Colorectal cancer (CRC) is one of the most common adenocarcinomas and exhibits progressive increases of metastasis-related mortality every year (by 2% per year in people under 50 years and 1% per year in people 50-64

years ([Kim et al., 2020](#), [Rawla et al., 2019](#), [Howlader et al., 2022](#)). The Cancer Genome Atlas indicates that the expression of Vim, Myo10 or both leads to an unfavorable prognosis in cancer and that overexpression of Vim decreased ($p=0.02$) patient survival in colorectal adenocarcinoma (NCI, 2022). There are no data on the impact of simultaneous overexpression of Vim and Myo10. Accordingly, we performed immunohistochemistry of 26 tissue samples obtained from the Ontario Tumor Bank that exhibited discrete stages of cancer progression (low to high grade). All samples were processed under standardized conditions to minimize results variations due to processing procedures and the precision of analysis was improved by drawing regions around the epithelial cells located on the border of the tumor area to the stroma to avoid inclusion of only stroma ([Rogojanu et al., 2015](#)). Quantification of a two-channel colocalization between Vim and Myo10 in normal tissue (Figure 1A) and tumor (Figure 1B) showed increased Pearson correlations between Vim and Myo10 in tumor specimens. Whereas the combined data from the different stages of tumor samples showed ~12.6-fold ($p=0.0089$) higher colocalization of these proteins in tumor epithelium, normal tissues from the same patients (Figure 1C) showed no differences in colocalization ($p=0.1477$) (Figure 1D). Analyses of the Myo10 mean fluorescence intensity (MFI) detected in epithelium and stroma showed ~62% ($p=0.0071$) higher MFI of Myo10 in epithelium than stroma (Figure 1E) and no significant differences between Myo10 signals from normal and tumor tissue from the stroma region ($p=0.4028$) and for Vim in epithelial ($p=0.6978$) and stromal ($p=0.4912$) regions (Figure 1F).

2. *Vimentin filaments regulate myosin 10 trafficking and localization*

For examining potential mechanisms, we utilized three types of mouse embryonic fibroblasts (mEFs; WT, Vim KO, and cells expressing Vim unit length filament, ULF) to analyze Vim- dependent spatial distributions of Myo10. Since many of these experiments were performed on cells of the fibroblast lineage, we extended our findings with data obtained from analyses of CRC SW480 cells (WT and Vim KD) that reflect Vim-Myo10 interactions in CRC tissue samples. As increased Vim and Myo10 expression are often associated with cancer metastasis ([Cao et al., 2014](#), [Courson and Cheney, 2015](#), [McInroy and Maatta, 2007](#), [Satelli and Li, 2011](#), [Strouhalova et al., 2020](#)), we assessed whether the pattern of Myo10 distribution was related to alterations of protein expression by immunoblotting whole cell lysates (Figure 2A). Time course experiments showed constant Myo10 expression for all mEF cell expressing Vim over 24h, but there were higher levels of Myo10 in KO cells ($p<0.02$, Figure S1A). A similar analysis of SW480 cells showed increased Myo10 over time (by ~22% between 3-24h; Figure S1A).

Analyses of confocal images showed that deletion of Vim in mEFs altered the location of Myo10 in cells plated on collagen (Col) (Figure S1B) and promoted the accumulation of Myo10 at the edge of cell extensions (Figure 2B). Analysis of the number of cell extensions with Myo10 aggregated at the tips versus the total number of extensions (Figure 2C) showed that deletion of Vim reduced the mean number of protrusions exhibiting aggregates of Myo10 at their tips by 45% ($p<0.0001$) compared with wild type controls. A point mutation in the Vim sequence that prevents the maturation of unit length filaments (ULF) to mature filaments ([Robert et al., 2015](#)) caused a time-dependent decrease of Myo10 accumulation at the tips (40%; $p<0.0001$). Further, analysis of Vim-rich SW480 cells (Figure S1C) showed robust suppression (by ~87%; $p<0.001$, Figure S1D) of tip-localized Myo10 after Vim KD compared with control siRNA.

We assessed whether Myo10 associates with soluble vimentin by immunoprecipitation of lysates prepared from

cells previously plated on Col, which showed that Myo10 associates with soluble vimentin (Figure 2D). The spatial relationship of Vim and Myo10 was examined in intact cells with stimulated emission depletion microscopy (STED). Super-resolution images of the tips of cell extensions showed that Vim aggregates were closely associated with Myo10 aggregates in mEF WT cells (Figure 2E). Quantification of immunostained images by Pearson correlation showed ~57% ($p < 0.0001$) colocalization of Vim with Myo10 for mEF WT cells. MEF ULF cells showed significantly lower Vim and Myo10 colocalization (36%; $p < 0.0001$ Figure 2F). We also examined Vim KO cells for potential non-specific interaction and found that the correlation of Myo10 with background Vim signal was 10-fold lower than WT cells. When the same analysis was applied to SW480 cells (Figure S1E), colocalization of Myo10 with Vim was reduced in Vim knockdown cells (by 46%, $p < 0.0001$; Figure S1F).

As immunoprecipitation and co-localization of immunostained samples do not provide direct evidence for interaction between Vim and Myo10, we used fluorescence resonance energy transfer (FRET) to examine binding in intact cells co-transfected with Myo10-GFP (donor) and Vim-RFP (acceptor) that were then plated on Col for 3h. Donor and acceptor pre- and post-bleach images (Figure 2G) were used to calculate mean FRET efficiencies. Consistent with the data from co-localization studies (Figure 2F), mEF WT exhibited the highest energy transfer efficiency ($E = \sim 40\% \pm 2.2\%$) between Vim and Myo10. In contrast, presumptive alterations in the equilibrium of Vim assembly and disassembly provoked a marked reduction in FRET efficiency in mEF ULF ($E = 19\% \pm 4.3\%$, Figure 2H). Vim interaction with full-length recombinant Myo10 was further characterized by surface plasmon resonance (SPR). SPR experiments were carried out with purified Myo10 immobilized on to an amine sensor chip (Nicoya). Analyses of Vim binding curves (Figure S1G) indicated that Vim tightly bound to immobilized Myo10 (mean \pm standard error $K_d = 57 \pm 0.029$ nM).

We analyzed whether Vim structure and solubility contribute to the interaction of Vim with Myo10. Cells were treated with IPA3, a specific p-21 kinase (PAK1) inhibitor ([Rudolph et al., 2013](#)) that strongly affects Vim assembly and cell extension formation ([Ostrowska-Podhorodecka et al., 2021](#)). Confocal imaging showed that IPA3 suppressed the trafficking of Myo10 into cell protrusions, strongly reduced the size of Myo10 aggregates at the extension tips and promoted the accumulation of Myo10 in the cell body (Figure 2I). Quantification of the size of Myo10 aggregates (measured by STED) showed that in cells with no or poorly developed Vim filaments (i.e., mEF KO or ULF), the size of Myo10 aggregates was reduced by ~40% ($p < 0.0097$) at the tips of cell extensions, which was not further reduced by IPA3 treatment (Figure 2J). In contrast, for mEF WT cells, IPA3 reduced the size of Myo10 aggregates by 53% ($p < 0.0018$) compared with untreated WT cells. SW480 cells, which mainly express insoluble Vim filaments, showed similar sizes of Myo10 aggregates and reduction after IPA3 treatment (~47%, $p < 0.0007$). Collectively these data indicate that mature Vim filaments promote the aggregation of Myo10 at the tips of cell extensions.

We examined whether increased Vim solubility may impact Vim-Myo10 interactions. Treatment with IPA3 did not markedly affect the interaction between Vim and Myo10 in mEF cells in whole cell lysates. Immunoprecipitation of Myo10 that associated with Vim after IPA3 treatment was increased by 76% ($p = 0.0024$; adjusted for Myo10 input) for SW480 cells (Figure 1K, L). Changes of Vim solubility induced by IPA3 in SW480 cells promoted a 50% increase of Vim that immunoprecipitated Myo10 ($p = 0.0198$; adjusted for Vim input; Figure 2K, M). These data likely reflect increased solubility of Vim in cytosol after IPA3 treatment that is consistent with aggregation of Myo10 particles in the

cell body (Figure 2I).

3. *Vimentin regulates myosin-10 dynamics*

As the abundance of Vim filaments affect the formation and stabilization of cell extensions during cell migration [Ding et al., 2020](#), [Ostrowska-Podhorodecka et al., 2021](#)), we evaluated the contribution of Vim to the movement of eGFP-tagged Myo10 by fluorescence recovery after photobleaching (FRAP). After 3 h of culture on fibrillar Col (1 mg/ml), cells were photobleached, and fluorescence recovery was measured for 150 s after bleaching (Figure 3A). All data were normalized to the non-bleached region of interest. Aggregated FRAP curves for each cell type (n=20 for each cell type) showed that cells with impaired Vim networks exhibited slower Myo10 fluorescence recovery (Figure 3B). Based on the pre- and post-bleaching measurements, we calculated the % mobile fraction and half-time (t_{1/2}) recovery of Myo10 aggregates. Depletion or reduction of Vim filaments (in KO or ULF cells) reduced the mobile fraction of Myo10 by 72% and 56% (respectively, p<0.0001, Figure 3C). Moreover, these alterations of Vim induced 2-fold slower half-time recovery (KO p<0.034 and ULF p<0.0078; Figure 3D). Further, reconstituted expression of Vim in mEF null cells completely restored the Myo10 mobility and fluorescence recovery time (compared with WT cells). KD of Vim in SW480 cells showed a similar trend in which the mobile fraction of Myo10 was reduced by 50% (p=0.0016) compared with untreated SW480 cells (Figures 3B, C). In addition, the mean recovery half-time for SW480 KD cells was ~63% (p=0.0016) lower than SW480 cells treated with control siRNA (Figure 3D).

Analysis of the velocity of Myo10 clusters in cell extensions (recorded over 5 min, frame/sec) by live-cell imaging (Figure S2A) showed that the processive movement of Myo10 was dependent on Vim expression. With the use of the Fiji tracking feature, we measured the velocity of Myo10 aggregates in cell extensions (n=35 extensions measured for each cell type plated on Col). Depletion of Vim was associated with 80% (p<0.0001) reduction of Myo10 velocity in cell extensions (Figure 3E; Figure S2B). Moreover, cells that expressed Vim ULF showed 25% (p=0.0174) slower Myo10 movement, which was consistent with FRAP data. Restoration of Vim expression by transfection with a Vim plasmid showed 3-fold higher (p=0.0035) Myo10 velocity compared with KO cells.

4. *Vimentin expression effects collagen reorganization and traction remodeling*

The data above showed that Vim affects Myo10 trafficking in cells plated on Col, but it is not known whether this association is required for Col remodeling. We quantified the effect of deleting Vim expression on cell-mediated Col remodeling by traction forces in cells cultured for 6 h in Col gels (1 mg/ml) and imaged by confocal reflection microscopy (Figure 4A). Collagen alignment was measured in fixed-size regions in the cell periphery and normalized to fixed-size areas in areas of the gels without cells. Compared with mEF WT cells, mEF KO and ULF exhibited ~45% (p<0.0006) and ~35% (p<0.0062) lower Col fiber alignment, respectively. On the other hand, re-expression of Vim increased alignment compared with Vim null cells (by 26%; p<0.015; Figure 4B). We analyzed the abundance of Col fibrils in discrete sampling grids to assess Col compaction, which showed that loss of Vim (in mEF cells) or depletion of Vim filaments (in ULF cells) reduced Col compaction (by ~26%; p<0.0001 and ~10% p<0.024, respectively; Figure 4C). Analyses of SW480 cells showed reduced Col alignment (~36%; p<0.0012) after Vim KD and Col fiber compaction (11% (p<0.0006; Figures 4B and C).

We assessed the impact of Myo10 KD (by Myo10 siRNA transfection) on Col remodeling (Figure 4D). Analysis of Vim-positive cells showed 33% ($p < 0.0012$) lower Col alignment after Myo10 deletion, which was similar to data obtained for mEF Vim KO cells (31%; $p < 0.0124$). Treatment of Vim KO cells with Myo10 siRNA did not further affect Col remodeling (Figure 4E). Measures of Col compaction showed a similar trend after KD of Myo10 (~ 20% reduction; $p < 0.0001$ compared with WT control and mEF KO cells; Figure 4F). Reduction of Myo10 in mEF KO cells did not change Col compaction. These results indicate that intact Vim filaments are important for cell-directed Col deformation associated with cell migration and with Vim-Myo10- dependent Col remodeling.

Fibrillar Col in connective tissues are organized into complex and diverse hierarchical networks [Fang et al., 2012](#)). We examined whether Col fiber structure was affected by Vim expression (Vim WT or Vim null) and the presence of Vim filaments (Vim WT or SW480 cells). We quantified D-spacing in collagen fibrils at the micrometer to sub-micrometer scale by Atomic Force Microscopy (AFM) imaging and two-dimensional Fast Fourier Transform (2D FFT) analysis. AFM images (Figure S3A) of mEF WT, KO and SW480 plated on Col gels showed that fibrils from different cell types exhibited distinctively different D-spacings. Compared with WT cells, deletion of Vim resulted in a small but significant (5%; KO $p < 0.0065$) reduction of the width of D-bands immediately underlying cells (Figure S3B). Collectively, these data suggested that Vim expression affects discrete structural aspects of Col fibers.

We examined the contribution of Vim to Col tractional remodeling by seeding cells at low density on to Col gels containing paramagnetic beads (2 mm diameter) as positional markers. Collagen substrate deformation was calculated from bead displacements (Figure 4G) using particle image velocimetry for 0–5 h after cell attachment ([Coelho et al., 2020](#)). Analysis of the resultant heat-color-coded vector map showed maximum collagen substrate deformations near the cell centroid. Deletion of Vim or the in cells that were unable to generate Vim filaments (ULF) was associated with a ~2-fold decrease of substrate deformation in KO and ULF cells compared with WT cells (KO $p < 0.0026$; ULF $p < 0.043$; Figure 4H).

Cell migration through soft connective tissue relies on Col remodeling [Arora et al., 2015](#), [Coelho et al., 2020](#), [Lu et al., 2011](#)). We examined whether Vim expression is required for Col proteolysis by quantifying degraded pericellular Col with neo-epitope antibodies that recognize 3/4 Col degradation fragments ([Yuda and McCulloch, 2018](#), [Wolf et al., 2007](#)). There was ~43% ($p < 0.0001$) reduced fluorescence intensity of immunostained degraded Col in fixed and permeabilized Vim KO cells compared with WT cells for mEF and SW480 cells. In contrast, cells expressing Vim ULF showed similar levels of degraded pericellular Col as WT cells (Figure 4I, and 4J), suggesting that Col proteolysis is dependent on Vim expression but not the formation of Vim filaments.

5. *Vimentin expression controls fibrillar collagen degradation by regulating MT1-MMP.*

The structure of native fibrillar Col contributes to its resistance to degradation by most proteases. But certain collagenases (MMP1, MMP8, MT1-MMP) exhibit triple helicase activity and can efficiently degrade fibrillar collagens ([Lee et al., 2019](#), [Lu et al., 2011](#)). As a result of its anchorage to the plasma membrane, MT1-MMP is particularly effective for pericellular Col proteolysis ([Marcink et al., 2019](#)). As Vim associates with the cytoplasmic tail of MT1-MMP in 3D endothelial cultures ([Kwak et al., 2012](#)), we examined whether Vim expression regulates the localization of immunostained MT1-MMP in non-permeabilized cells (Figure 5A). There was a 39% ($p < 0.0001$) reduction of the mean

plasma membrane-associated MT1-MMP fluorescence in Vim-deficient cells compared with WT cells. Expression of Vim ULF showed a smaller reduction (~19%) of MT1-MMP fluorescence compared with WT cells ($p=0.004$; Figure 5B).

We assessed whether intracellular trafficking of MT1-MMP is dependent on Vim and Myo10 expression. We performed FRAP assays for mEF WT and mEF Vim KO cells transfected with a GFP-MT1-MMP plasmid and that were co-transfected with Myo10 siRNA (the Myo10 KD efficiency is presented in Figure 5C). After 3h of cell culture on fibrillar Col, cells were photobleached and fluorescent recovery was recorded for 150 s (Figure 5D). Data were normalized as described above; aggregated FRAP curves for each cell type ($n=20$ for each cell type) are shown in Figure 5E. Calculation of half-time recovery showed that loss of Vim or Myo10 in cells resulted in 2.5-fold ($p<0.0012$ and $p<0.0066$, respectively) slower fluorescence recovery (Figure 5F). Concurrently, the relevant mobile fraction was ~28% ($p<0.0068$) lower for Vim KO cells compared with WT, and the depletion of Myo10 greatly reduced MT1-MMP mobility ($< 80%$, $p<0.0001$; Figure 5G).

As Myo10 colocalizes with MT1-MMP (Sun et al., 2019), we analyzed the membrane-associated fraction of immunostained MT1-MMP in non-permeabilized cells by flow cytometry (Figure 5H). Compared with WT cells, Vim KO cells exhibited 22% ($p<0.002$) reduction of membrane-associated MT1-MMP fluorescence. No detectable changes in the membrane fraction of MT1-MMP were found in ULF cells compared with WT cells ($p>0.53$). Further, we analyzed MT1-MMP levels by western blotting of focal adhesion complex proteins and of total cell lysates prepared from cells grown on Col (Figure 5I). MEF KO cells exhibited lower expression of MT1-MMP than WT, but there was a larger ($p<0.05$) fraction of activated MT1-MMP in the focal adhesion samples. Whereas ULF cells were not significant different from WT cells ($p>0.27$), which is consistent with the flow cytometry data (Figure 5J). These results suggested that Vim expression is involved in the MT1-MMP-dependent up-regulation of Col remodeling by migrating cells.

Discussion

Our major findings are that Vim impacts collagen remodeling by directly interacting with the cell extension tip marker, Myo10, and that Vim regulates Myo10 trafficking at the cell extension tip, which enhances tractional remodeling (Figure 6). This process may be of considerable importance in cell migration. These data illuminate how Vim is related to EMT, a biological phenomenon in which non-migratory epithelial cells acquire the migratory behavior of mesenchymal cells. As increased Vim expression and reduced cytokeratin are hallmarks of EMT progression (Acloque et al., 2009, De Craene and Berx, 2013, Nieto et al., 2016), our data advance understanding of EMT, which could facilitate the development of novel therapeutics for fibrosis (Rout-Pitt et al., 2018) and many types of human cancers (Nieto, 2009, Thiery et al., 2009, Rawla et al., 2019).

Colorectal cancer (CRC) is one of the most common malignancies in developed countries and remains a major cause of death (Kim et al., 2020). The overexpression of Vim filaments is associated with CRC metastasis and poor prognosis (McInroy and Maatta, 2007, Toiyama et al., 2013, Lazarova and Bordonaro, 2016). Our analysis of human CRC tissues indicated a positive correlation between Vim and Myo10 colocalization in tumor epithelium. Our findings suggest that the Vim-Myo10 interaction is correlated with cancer progression. Deeper insights into this phenomenon may open new possibilities for drug development. Thus, the interaction between Vim and Myo10 might provide a new potential target for CRC treatment.

Previous data demonstrate that the number and length of filopodia are directly regulated by Myo10 ([Plantard et al., 2010](#), [Margiotta et al., 2017](#)) and by Vim filaments ([Ostrowska- Podchorodecka et al., 2021](#)). To the best of our knowledge, no published data indicate that Vim directly interacts with Myo10 to modulate cell migration-dependent matrix remodeling. We found that Vim complexed with Myo10 at the tips of cell extensions and that depletion of Vim strongly impacts Myo10 localization, which then causes accumulation of Myo10 behind the leading edge of migrating cells. These data underline an essential regulatory role of Vim in Myo10-dependent cell extension formation.

Soluble Vim immunoprecipitates with NMIIA/B ([Menko et al., 2014](#)), which is similar to our data of Vim and Myo10. Vimentin filaments undergo dynamic reorganization during cell motility and Vim oligomers (ULFs) rapidly exchange subunits with the soluble vimentin pool ([Robert et al., 2016](#)). However, we found that the Vim-Y117L mutant (ULF cells) showed limited interaction with Myo10, suggesting that residues in the N-terminal of Vim may contain a Myo10 binding site. These data corroborate and are consistent with our FRET experiment showing lower energy transfer in ULF cells. Further, our SPR data showed high-affinity binding of soluble recombinant Vim with full-length Myo10. Notably, the Kd estimated from SPR data (57 nM) is similar to Kds obtained for Vim binding to a membrane glycoprotein CD44 (SPR-37 nM and isothermal titration calorimetry – 74 nM) ([Pall et al., 2011](#)).

Colon cancer SW480 cells show a high level of Vim expression ([Zeindl-Eberhart et al., 2014](#), [Toiyama et al., 2013](#)). We found that most of the Vim in these cells is present as insoluble filaments; only a small fraction was soluble. When we inhibited PAK-1 activity with IPA3, an intervention that increases the pool of soluble Vim ([Rudolph et al., 2013](#), [Ding et al., 2020](#)), we found increased Vim-Myo10 association. We also discovered that perturbation of Vim filament structure by IPA3 resulted in the retraction of Myo10 from cell extensions to the cell body, further supporting a role for Vim filament assembly in the trafficking of Myo10 toward the tips of cell extensions.

Previous FRAP analyses of single Vim filaments in the periphery of cells showed fast retrograde movement (~520 nm/s) ([Leduc and Etienne-Manneville, 2015](#)). Intra-filopodial single- molecule movement of Myo10 is estimated at 461 ± 277 nm/s ([Watanabe et al., 2010](#)). The similarity of these data suggests that Vim and Myo10 may move together during filopodial formation and is consistently with our data indicating depletion of Vim reduced the mobility of Myo10 in cell extensions.

Vim expression is associated with increased collagen accumulation and re-epithelialization of healing wounds ([Cheng et al., 2016](#), [Cheng and Eriksson, 2017](#)). Our findings corroborate and are consistent with previous data demonstrating that Vim-deficient fibroblasts exhibit reduced collagen contraction compared with wild-type cells ([Eckes et al., 2000](#), [Eckes et al., 1998](#)). In addition, we found that the fibril D-spacing was affected by Vim expression and possibly by the interaction of Vim with Myo10. Extensively crosslinked collagen fibrils and subsequent stiffening of the ECM can lead to increased invasion of cancer cells ([Levental et al., 2009](#), [Yu et al., 2011](#), [Coelho et al., 2020](#)). Consequently, the growth of CRC cells leads to collagen compaction ([Delaine- Smith et al., 2019](#)), which is consistent with our data showing that SW480 cells avidly contract and compact collagen, and that this process is suppressed by Vim deletion.

Collagen degradation is mediated by specific MMPs such as MT1-MMP, which are expressed by cells at the wound site ([Cox and Erler, 2011](#)). We found that Vim expression regulates collagen degradation through Myo10-dependent control of MT1-MMP secretion. Earlier data indicate that Myo10 plays a role in ECM degradation as Myo10 localizes to podosomes in osteoclasts ([McMichael et al., 2010](#)). Moreover, strong colocalization of MT1-MMP with Myo10 in

presumptive podosomes suggests a key role of Myo10 in collagen degradation ([Sun et al., 2019](#)). Further, the catalytic activity of certain proteases (MMP2, MT1-MMP) is reduced when Myo10 is silenced in breast cancer tumors ([Cao et al., 2014](#)). Notably, Vim is required for surface translocation of MT1-MMP in endothelial cell sprouting ([Kwak et al., 2012](#)). Consistent with these data we found that loss of Vim disables MT1-MMP translocation to the plasma membrane because of abrogation of Myo10 trafficking.

In summary we provide the first demonstration of a crucial role for the binding of Vim to Myo10 in regulating Myo10 trafficking and targeting MT1-MMP-dependent Col proteolysis. Collectively these processes strongly impact matrix remodeling and cancer cell invasion of soft connective tissues. Future studies are needed to assess whether suppression of the Vim-Myo10 interaction affects the progression of colon cancer.

Materials and Methods

Reagents and antibodies

Goat anti-rabbit IgG H&L (DyLight® 488) (ab150077), rabbit anti-vimentin (EPR3776, ab92547), rabbit anti-MT1-MMP (EPI264Y, ab51074) antibodies, 100x Citrate Buffer pH 6.0 (Antigen Retrieval Buffer; ab9367), Sea Block Serum free, PBS (# 166955) were purchased from Abcam (Cambridge, MA). Rabbit anti-Collagen Type 1 (3/4 fragment), pAb (0217-050) was from (ImmunoGlobe Antikörpertechnik GmbH, German). Chicken anti-vimentin antibody (N13300-223) was purchased from Novus Biologicals (Littleton, CO). Mouse anti- β -actin (A1978) and rabbit anti-myosin 10 (HPA024223) antibodies, DAPI were obtained from Sigma-Aldrich (St. Louis, MO). Alexa Fluor® 488 goat anti-mouse (A11001), Alexa Fluor® 568 goat anti-rabbit (A-11011) secondary antibodies, and rhodamine phalloidin, were from (Invitrogen, Carlsbad, CA, USA). Alexa Fluor® 647 AffiniPure F(ab')₂ fragment donkey anti-chicken IgY (H+L) (703-605-155) secondary antibody was from Jackson ImmunoResearch (West Grove, PA). BCA protein assay (Pierce), RIPA lysis and IP lysis buffer and Lipofectamine 3000 reagent were obtained from ThermoFisher Scientific (Mississauga, ON). Type I Bovine Collagen Solution (3 mg/ml and 6 mg/ml) was from Advanced BioMatrix (San Diego, CA). Plasmids containing pEGFP-Myo10 (#87256), mTagRFP-T-Vimentin (#58029) were obtained from Addgene (Cambridge, MA). ON-TARGETplus Non-target Pool 5 nmol, ON-TARGETplus siRNA Reagents-VIM 5 nmol were obtained from Horizon (Lafayette, CO). Mouse Myo10_6 FlexiTube siRNA (ID SI04252822) was purchased from GeneGlobe (Qiagen) (Germantown, MD, USA). Recombinant full-length Myo10 was obtained from Creative BioMart (Shirly, NY, USA). Recombinant Vim was a kind gift from P.A. Janmey (University of Pennsylvania, PA, US).

Cell culture and transfection

Vimentin-positive mouse embryonic fibroblasts (mEF WT) and vimentin-null (mEF KO) were derived from wild type and vimentin knockout mice, that were originally isolated by J. Ericsson (Abo Akademi University, Turku, Finland); mEFs expressing unit length filaments (ULF) were obtained from V. Gelfand (Northwestern University, Chicago, USA). This cell type contains a point mutation (Y117L) in Vim, which results in the inability of Vim to polymerize into filaments. SW480 cells, which are a cancer line that express vimentin filaments, were obtained from ATCC. All cells were cultured at 37°C in complete DMEM containing 10% FBS, penicillin 100 U/mL, and streptomycin 100 μ g/mL. For vimentin siRNA transfection cells were trypsinized and plated on 6 well plate to 60-70% confluence. Vim re-expression was done by co-transfection

with vim- containing plasmids. To obtain Vim or Myo10 KD, cells were transfected with respective siRNAs using Lipofectamine 3000. As a transfection control cell were treated with non-target control Dharmacon ON-TARGET plus transfection reagents according to the manufacturer. Cells were grown for 48 h, lysed in the RIPA buffer, and whole-cell lysates were collected. Protein concentrations were determined by the BCA protein assay (Pierce). Equal amounts of proteins from each treatment condition were separated on 8% acrylamide gels and immunoblotted to estimate the efficiency of the KD.

Immunoblotting

Cells were plated on collagen-coated 100 mm dishes and lysed with RIPA buffer (25 mM Tris- HCl pH 7.6, 150 mM NaCl, 1% NP-40, 1% sodium deoxycholate, 0.1% SDS) supplemented with 1 mM PMSF, 1 mM NaVO₃, 10 µg/ml protease inhibitor cocktail. Equal amounts of proteins were loaded on 8% polyacrylamide gels, resolved by SDS/PAGE and transferred to nitrocellulose membranes for 18 h. The membranes were blocked with 5% BSA-TBS for 1 h followed by overnight incubation with primary antibodies. Membranes were washed and incubated with respective secondary antibodies for 1 h in TBS supplemented with 0.1% Tween-20 at room temperature. All immunoblots were performed in triplicate. Blots were visualized with a Li-Cor Odyssey imager (Lincoln, NB) and quantified by densitometry with ImageJ software.

Immunostaining and microscopy analysis

In experiments, cells were cultured on collagen (fibrillar;1 mg/ml), fixed with 1% PFA for 15 min, permeabilized in 0.2% Triton X-100 for 10 min, and blocked with 1% BSA. Samples were incubated with appropriate primary antibodies for 1 h at 37°C. Cells were washed with PBS and stained with secondary antibody as indicated. In most experiments, cells were stained with DAPI (10 µg/ml) and rhodamine-phalloidin for actin filaments. Images were obtained with a TCS SP8 confocal microscope (Leica Microsystems, Wetzlar, Germany) equipped with a ×40 oil-immersion objective lens, Zeiss LSM 800 Confocal (Germany) and STEDYCON, capable of achieving lateral STED resolution of <40nm, depending on dyes used. Mounted on an inverted Leica DMI6000B microscope. Analysis and quantification of acquired images were done with ImageJ software. The cell outline was determined using the cell outliner plugin (<https://imagej.nih.gov/ij/plugins/cell-outliner.html>). Pearson correlation coefficients were determined with JACoP (Just Another Colocalization Plugin) (<https://imagej.nih.gov/ij/plugins/track/jacop.html>) in Fiji. The number and area of Myo10 particles were quantified on fluorescence images acquired by STED microscope according to the method described in (Coelho et al., 2017). The number and area of Myo10 particles were obtained with the Analyze Particles program in Fiji.

Förster Resonance Energy Transfer (FRET)

Acceptor Photobleaching-FRET was performed on a Leica SP8 confocal microscope with the Leica AP-FRET mode. Photo-bleaching was minimized during acquisition by using low laser power (10% for 488 nm and 552 nm). A region of interest (ROI; 1×1 µm) was chosen in selected areas and 100% laser power was used with eight iterations for photo-bleaching the acceptor mFRP–Vim. Pre-bleach and post-bleach images were acquired using the same settings. The efficiency of energy transfer (E%) was calculated using the equation: $E\% = (\text{Donor post-bleach} - \text{Donor pre-bleach}) \times 100 /$

(Donor post-bleach).

Surface plasmon resonance (SPR) measurement

Nicoya (Lifesciences) OpenSPR was used to measure interactions of immobilized Myo10 with recombinant vimentin as an analyte. As a running buffer PBS (phosphate buffered saline pH 7.4) was applied, at a flow rate of 20 μ l/min at RT. Myo10, 10 μ g/ml in Activation Buffer, was immobilized on an Amine sensor chip using EDC/NHS coupling kit according to the manufacturer's instruction. Vimentin in PBS was added at different concentrations ranging from 0.25 to 2 M were injected in the flow channel with immobilized Myo10, and dissociation was recorded for 300 s. Selection of the concentrations used for Vim depended on the signal obtained from injected analyte. Each Vim injection step was followed by a regeneration step (injections of 10 mM Glycine/HCl pH 1.5 for 300 s). Each sensogram was corrected for the bulk injection of 5 μ M BSA in PBS buffer and a signal from the PBS flow channel. Data were analyzed with TraceDrawer software. One state model was fit to each binding curve to calculate association (k_a) and dissociation (k_d) rate constants. The apparent equilibrium binding constant (KD) was calculated by dividing k_d by k_a obtained from each sensogram.

Fluorescence recovery after photobleaching (FRAP)

FRAP analysis was performed as described in [Coelho et al., 2020](#). Briefly, FRAP was performed using Leica TCS SP8 confocal microscope in the FRAP module. Cells transiently transfected with eGFP-Myo10 plasmid were cultured for 6 h on either collagen or fibrinogen. In FRAP experiments the region of interest (ROI; $1 \times 1 \mu$ m) was photobleached and fluorescent recovery was monitored for 180 s after. Images were analyzed with FIJI software. To compensate for cell drift, the Linear Stack Alignment with SIFT plug-in was used. Fluorescence value measurements were then exported to Microsoft Excel where they were normalized and scaled between 0–1 using:

$$I_{norm} = \frac{[(I_{bleach} - I_{nonbleach}) - \max(I_{bleach} - I_{nonbleach})]}{\max(I_{bleach} - I_{nonbleach}) - \min(I_{bleach} - I_{nonbleach})}$$

To perform curve fitting analysis, plot, and do statistical analysis of the various parameters obtained from the double exponential equation we utilized GraphPad Prism (San Diego, CA, USA).

Atomic force microscopy analysis

Fibrillar collagen substrates were prepared from pepsin-solubilized bovine dermal type I atelocollagen. Stock collagen solutions were diluted to a final concentration of 1mg/mL and neutralized with 0.1M NaOH to pH=7.4. Prior to the addition of collagen solutions, MatTek 50mm glass bottom culture dishes were exposed to oxygen plasma, followed by immediate coating with 2% APTES and 0.1% v/v glutaraldehyde, washed and air-dried. Collagen solutions were then added to the center of the glass well and covered with an untreated glass coverslip. After collagen polymerization at 37°C in 5% CO₂ for 90 min, coverslips were gently detached from the fibrillar collagen gel by warm PBS. Cells were added directly on top of the collagen gel and incubated at 37°C in 5%CO₂ until filopodial initiation began (>3hrs). They were fixed with 4%PFA,

permeabilized with 0.2% TritonX-100, and washed with 1xPBS. Extensive washing with deionized water was also performed before air-drying thoroughly at room temperature. Imaging was carried out in ambient conditions on a MultiMode AFM with Nanoscope III controller (Digital Instruments, Santa Barbara) and silicon cantilevers (OTESPA-R3, Bruker AFM probes, Santa Barbara, CA, USA). The amplitude set point was adjusted to 75% of the default to minimize potential damage to the collagen structure.

Collagen remodeling

Glass-bottom 50 mm dishes were sterilized with UV light, coated with 2% APTES (Sigma-Aldrich) and washed extensively with distilled water, and immersed in 0.1% glutaraldehyde (Caledon Laboratories, Canada). Then dishes were coated with fibrillar collagen (1 mg/ml), which was left to polymerize for 1 h at 37°C. Cells were plated on collagen-coated substrates for 5 h before fixing with 4% paraformaldehyde for 10 min and being permeabilized with 0.2% Triton X-100 for 10 min. Fibrillar collagen images were quantified to provide estimates of the remodeling activity using two approaches: compaction (fibril intensities) and reorganization (alignment index) of collagen fibers around cell extensions ([Coelho et al., 2020](#)). To determine collagen compaction collagen fibrils intensities in fixed areas around the cell extensions were measured in each sample and normalized against collagen intensities in samples without cells. Local collagen fiber alignment was quantified using Fast Fourier Transform (FFT) and Oval Profile (ImageJ plug-in) as described earlier ([Mohammadi et al., 2015](#)).

Collagen tractional remodeling

Widefield microscopy (Zeiss Axiovert 135) was used to image collagen tractional remodeling in environmentally controlled conditions (37°C/5% CO₂). Cells were cultured at low density into collagen gels (1 mg/mL) with 2µm diameter polystyrene microbeads. Cells (mEF WT, mEF vim KO and ULF) were then plated on the collagen gels. The initial bead position was determined 1 h after cell seeding, when cells were properly attached to the gel surface. A time series of 120 images was collected at a frequency of one image every 5 min. Image stacks were aligned using Image J plug-in Linear Stack Alignment with scale-invariant feature transform (https://imagej.net/Linear_Stack_Alignment_with_SIFT). Collagen deformation was calculated from bead displacements using particle image velocimetry (PIV) for 0–5h after cell attachment.

Flow cytometry

For quantification of the membrane-associated MT1-MMP cells were plated on collagen (1 mg/ml)-coated 100 mm dishes for 3 h (Segal et al., 2001). Cells were washed and incubated with primary antibodies (rabbit anti-MT1-MMP) for 1 h in 37°C on live cells. Cells were washed with ice-cold PBS, scraped immediately with Versene solution and fixed with 1% PFA. Cells were washed with PBS, stained with FITC-conjugated anti-rabbit secondary antibodies and analyzed by flow cytometry (Sony SA3800 Spectral Analyzer).

Immunoprecipitation

Cells were cultured on collagen-coated 150mm dishes for 3h and lysed in IP lysis buffer (25 mM Tris-HCl pH 7.4, 150 mM

NaCl, 1 mM EDTA, 1% NP-40 and 5% glycerol) containing 1 mM PMSF, 1 mM NaVO₃, 10 µg/ml leupeptin, and 10 µg/ml aprotinin. Equal amounts of protein from cleared extracts were immunoprecipitated with the Dyna-beads® Protein G (Life Technologies) according to the manufacturer's protocol (Invitrogen, Carlsbad, CA, USA) with primary antibodies as indicated. Beads were separated by magnetic stand and washed 2x with an IP buffer. Beads were resuspended in 2x Laemmli sample buffer and boiling for 10 min for immunoprecipitated proteins elution. Clear lysates were analyzed by western blot.

Isolation of focal adhesion proteins

Cells were cultured to 80–90% confluence on 100 mm tissue culture dishes and then incubated with 1 mg/ml collagen-coated magnetite beads. Focal adhesion complexes were isolated from cells as described (Wang et al., 2009). In brief, cells were washed with ice-cold PBS to remove unbound beads and scraped into ice-cold cytoskeleton extraction buffer (CKSB; 0.5% Triton X-100, 50 mM NaCl, 300 mM sucrose, 3 mM MgCl₂, 20 µg/ml aprotinin, 1 µg/ml leupeptin, 1 µg/ml pepstatin, 1 mM phenylmethylsulfonyl fluoride, and 10 mM PIPES, pH 6.8). The cell-bead suspension was briefly sonicated, and the beads were isolated from the lysate using a magnetic separation stand. The beads were resuspended in fresh ice-cold CKSB and re-isolated magnetically. Then, beads were washed in CSKB, sedimented with a centrifuge, resuspended in 2x Laemmli sample buffer, and boiled for 10 min. The beads were separated magnetically, and lysates were analyzed by western blot.

Patient samples and tissue immunofluorescence stain:

All cases were selected from the archives of the Ontario Tumor Bank (Ontario Institute for Cancer Research). A total of 13 patients had CRC with previous biopsies at the colon site of the primary tumor. After the original diagnoses, all cases were reviewed by two pathologists (MM and AA from the author list) to determine the differentiation of adenocarcinoma. The final diagnoses were: Well-differentiated (low grade; LG; n=3), moderately differentiated (intermediate grade; IG; n=6); poorly differentiated (high grade; HG; n=1). Three samples were diagnosed as moderately/poorly differentiated adenocarcinoma. Each obtained tumor sample has a relevant normal tissue control from the same patient. Frozen tissue was cut for 7 µm sections from each OCT block. Slides were stained according to the protocol described in (Ali et al., 2021) with some modifications. Briefly, slides were heated to 60°C for 1 min and then fixed by incubations in 95% ethanol (30-sec), 10% formalin (30-sec), then water. Next, slides were immersed in antigen retrieval buffer at 98°C for 1h, Samples were cooled down in room temperature for 10 minutes and washed with warm water for 1 minute, dried, marked with Pap-pen and covered with TBS-T. Then tissue samples were permeabilized with 0.5% Triton (X100-Bioshop) for 5 min. The samples were washed with TBS- T three times and then incubated in sea blocking buffer (Sea Block Serum free-PBS abcam-UK) for 2h, followed by the overnight incubation with primary antibodies at 4°C. Next, slides were washed and incubated with secondary antibody, and after 1h incubation at room temperature, slides were washed again 3 times with TBS-T 5 minutes each and stained with DAPI for another 30 min. The samples were washed 3 times and finally mounted using ProLong Diamond Antifade Mounting media (Thermo Fisher Scientific) and imaged the same day using a Zeiss LSM 800 Confocal (Germany) equipped with a ×20 objective lens.

Research ethics

All methods and experiments follow the University of Toronto research guidelines. Ethical approval was obtained from the University of Toronto Research Ethics Board #32822.

Statistical analysis

Statistical significance ($p < 0.05$) was determined using the unpaired t-test for two samples or analysis of variance (ANOVA) for multiple samples. For analysis of the spatial relationship of proteins in cultured cells, Pearson correlation was used (Bolte and Cordelieres, 2006). Analyses were performed with GraphPad Prism 9 software. All experiments were performed at least three independent times in triplicates on separate days. Histograms display means and SEM.

Acknowledgments

The authors thank Dr. V.I. Gelfand from Northwestern University, Chicago, USA for kindly provision of mEF Vim-Y117L mutant (ULF cells). The authors thank the BioRender.com

Credit authorship contribution statement

Z. Ostrowska-Podhorodecka: Conceptualization, data curation, formal analysis, investigation, methodology, validation, visualization, writing - original draft, review, and editing. M. Norouzi: Data curation, validation, writing - review and editing. I. Ding, S. Abbasi, P. Arora, T. Wong, A. Ali: Data curation, validation. M. Magalhaes supervision, validation, visualization, writing - review and editing. C.A. McCulloch: Conceptualization, funding acquisition, investigation, methodology, project administration, resources, supervision, validation, visualization, writing - original draft, review, and editing.

References

- ACLOQUE, H., ADAMS, M. S., FISHWICK, K., BRONNER-FRASER, M. & NIETO, M. A. 2009. Epithelial-mesenchymal transitions: the importance of changing cell state in development and disease. *J Clin Invest*, 119, 1438-49.
- ALI, A., SOARES, A. B., EYMAEL, D. & MAGALHAES, M. 2021. Expression of invadopodia markers can identify oral lesions with a high risk of malignant transformation. *J Pathol Clin Res*, 7, 61-74.
- ALMAGRO, S., DURMORT, C., CHERVIN-PETINOT, A., HEYRAUD, S., DUBOIS, M., LAMBERT, O., MAILLEFAUD, C., HEWAT, E., SCHAAL, J. P., HUBER, P. & GULINO-DEBRAC, D. 2010. The motor protein myosin-X transports VE-cadherin along filopodia to allow the formation of early endothelial cell-cell contacts. *Mol Cell Biol*, 30, 1703-17.
- APLIN, A. C., ZHU, W. H., FOGEL, E. & NICOSIA, R. F. 2009. Vascular regression and survival are differentially regulated by MT1-MMP and TIMPs in the aortic ring model of angiogenesis. *Am J Physiol Cell Physiol*, 297, C471-80.
- ARORA, P. D., WANG, Y., BRESNICK, A., JANMEY, P. A. & MCCULLOCH, C. A. 2015. Flightless I interacts with NMMIIA to promote cell extension formation, which enables collagen remodeling. *Mol Biol Cell*, 26, 2279-97.
- BERG, J. S. & CHENEY, R. E. 2002. Myosin-X is an unconventional myosin that undergoes intrafilopodial motility. *Nat*

Cell Biol, 4, 246-50.

- BRABLETZ, T., HLUBEK, F., SPADERNA, S., SCHMALHOFER, O., HIENDLMEYER, E., JUNG, A. & KIRCHNER, T. 2005. Invasion and metastasis in colorectal cancer: epithelial-mesenchymal transition, mesenchymal-epithelial transition, stem cells and beta-catenin. *Cells Tissues Organs*, 179, 56-65.
- CAO, R., CHEN, J., ZHANG, X., ZHAI, Y., QING, X., XING, W., ZHANG, L., MALIK, Y. S., YU, H. & ZHU, X. 2014. Elevated expression of myosin X in tumours contributes to breast cancer aggressiveness and metastasis *Br J Cancer*, 111, 539-50.
- CHENG, F. & ERIKSSON, J. E. 2017. Intermediate Filaments and the Regulation of Cell Motility during Regeneration and Wound Healing. *Cold Spring Harb Perspect Biol*, 9.
- CHENG, F., SHEN, Y., MOHANASUNDARAM, P., LINDSTROM, M., IVASKA, J., NY, T. & ERIKSSON, J. E. 2016. Vimentin coordinates fibroblast proliferation and keratinocyte differentiation in wound healing via TGF-beta-Slug signaling. *Proc Natl Acad Sci U S A*, 113, E4320-7.
- COELHO, N. M., WANG, A., PETROVIC, P., WANG, Y., LEE, W. & MCCULLOCH, C. A. 2020. MRIP Regulates the Myosin IIA Activity and DDR1 Function to Enable Collagen Tractional Remodeling. *Cells*, 9.
- COURSON, D. S. & CHENEY, R. E. 2015. Myosin-X and disease. *Exp Cell Res*, 334, 10-5.
- COX, T. R. & ERLER, J. T. 2011. Remodeling and homeostasis of the extracellular matrix: implications for fibrotic diseases and cancer. *Dis Model Mech*, 4, 165-78.
- DANIELSSON, F., PETERSON, M. K., CALDEIRA ARAUJO, H., LAUTENSCHLAGER, F. & GAD, A. K. B. 2018. Vimentin Diversity in Health and Disease. *Cells*, 7.
- DE CRAENE, B. & BERX, G. 2013. Regulatory networks defining EMT during cancer initiation and progression. *Nat Rev Cancer*, 13, 97-110.
- DELAINE-SMITH, R., WRIGHT, N., HANLEY, C., HANWELL, R., BHOME, R., BULLOCK, M., DRIFKA, C., ELICEIRI, K., THOMAS, G., KNIGHT, M., MIRNEZAMI, A. & PEAKE, N. 2019. Transglutaminase-2 Mediates the Biomechanical Properties of the Colorectal Cancer Tissue Microenvironment that Contribute to Disease Progression. *Cancers (Basel)*, 11.
- DING, I., OSTROWSKA-PODHORODECKA, Z., LEE, W., LIU, R. S. C., CARNEIRO, K., JANMEY, P. A. & MCCULLOCH, C. A. 2020. Cooperative roles of PAK1 and filamin A in regulation of vimentin assembly and cell extension formation. *Biochim Biophys Acta Mol Cell Res*, 1867, 118739.
- ECKES, B., COLUCCI-GUYON, E., SMOLA, H., NODDER, S., BABINET, C., KRIEG, T. & MARTIN, P. 2000. Impaired wound healing in embryonic and adult mice lacking vimentin. *J Cell Sci*, 113 (Pt 13), 2455-62.
- ECKES, B., DOGIC, D., COLUCCI-GUYON, E., WANG, N., MANIOTIS, A., INGBER, D., MERCKLING, A., LANGA, F., AUMAILLEY, M., DELOUVEE, A., KOTELIANSKY, V., BABINET, C. & KRIEG, T. 1998. Impaired mechanical stability, migration and contractile capacity in vimentin-deficient fibroblasts. *J Cell Sci*, 111 (Pt 13), 1897-907.
- FANG, M., GOLDSTEIN, E. L., TURNER, A. S., LES, C. M., ORR, B. G., FISHER, G. J., WELCH, K. B., ROTHMAN, E. D. & BANASZAK HOLL, M. M. 2012. Type I collagen D-spacing in fibril bundles of dermis, tendon, and bone: bridging between nano- and micro-level tissue hierarchy. *ACS Nano*, 6, 9503-14.
- GREGOR, M., OSMANAGIC-MYERS, S., BURGSTALLER, G., WOLFRAM, M., FISCHER, I., WALKO, G., RESCH, G.

- P., JORGL, A., HERRMANN, H. & WICHE, G. 2014. Mechanosensing through focal adhesion-anchored intermediate filaments. *FASEB J*, 28, 715-29.
- HELFAND, B. T., MENDEZ, M. G., MURTHY, S. N., SHUMAKER, D. K., GRIN, B., MAHAMMAD, S., AEBI, U., WEDIG, T., WU, Y. I., HAHN, K. M., INAGAKI, M., HERRMANN, H. & GOLDMAN, R. D. 2011. Vimentin organization modulates the formation of lamellipodia. *Mol Biol Cell*, 22, 1274-89.
 - HIRANO, Y., HATANO, T., TAKAHASHI, A., TORIYAMA, M., INAGAKI, N. & HAKOSHIMA, T. 2011. Structural basis of cargo recognition by the myosin-X MyTH4-FERM domain. *EMBO J*, 30, 2734-47.
 - HOWLADER, N., NOONE, A. M., KRAPCHO, M., MILLER, D., BREST, A., YU, M., RUHL, J., TATALOVICH, Z., MARIOTTO, A., LEWIS, D. R., CHEN, H. S., FEUER, E. J. & CRONIN, K. A. 2022. *Key Statistics for Colorectal Cancer* [Online]. Atlanta, Ga. Available: <https://www.cancer.org/cancer/colon-rectal-cancer/about/key-statistics.html> [Accessed].
 - KAIMORI, A., POTTER, J., KAIMORI, J. Y., WANG, C., MEZEY, E. & KOTEISH, A. 2007. Transforming growth factor-beta1 induces an epithelial-to-mesenchymal transition state in mouse hepatocytes in vitro. *J Biol Chem*, 282, 22089-101.
 - KIM, T. W., LEE, Y. S., YUN, N. H., SHIN, C. H., HONG, H. K., KIM, H. H. & CHO, Y. B. 2020. Correction: MicroRNA-17-5p regulates EMT by targeting vimentin in colorectal cancer. *Br J Cancer*, 123, 1204.
 - KWAK, H. I., KANG, H., DAVE, J. M., MENDOZA, E. A., SU, S. C., MAXWELL, S. A. & BAYLESS, K. J. 2012. Calpain-mediated vimentin cleavage occurs upstream of MT1-MMP membrane translocation to facilitate endothelial sprout initiation. *Angiogenesis*, 15, 287-303.
 - LAM, V. K., NGUYEN, T. C., CHUNG, B. M., NEHMETALLAH, G. & RAUB, C. B. 2018. Quantitative assessment of cancer cell morphology and motility using telecentric digital holographic microscopy and machine learning. *Cytometry A*, 93, 334-345.
 - LAMOUILLE, S., XU, J. & DERYNCK, R. 2014. Molecular mechanisms of epithelial-mesenchymal transition. *Nat Rev Mol Cell Biol*, 15, 178-96.
 - LAZAROVA, D. L. & BORDONARO, M. 2016. Vimentin, colon cancer progression and resistance to butyrate and other HDACis. *J Cell Mol Med*, 20, 989-93.
 - LEDUC, C. & ETIENNE-MANNEVILLE, S. 2015. Intermediate filaments in cell migration and invasion: the unusual suspects. *Curr Opin Cell Biol*, 32, 102-12.
 - LEE, Y. H., SEO, E. K. & LEE, S. T. 2019. Skullcapflavone II Inhibits Degradation of Type I Collagen by Suppressing MMP-1 Transcription in Human Skin Fibroblasts. *Int J Mol Sci*, 20.
 - LEVENTAL, K. R., YU, H., KASS, L., LAKINS, J. N., EGEBLAD, M., ERLER, J. T., FONG, S. F., CSISZAR, K., GIACCIA, A., WENINGER, W., YAMAUCHI, M., GASSER, D. L. & WEAVER, V. M. 2009. Matrix crosslinking forces tumor progression by enhancing integrin signaling. *Cell*, 139, 891-906.
 - LU, P., TAKAI, K., WEAVER, V. M. & WERB, Z. 2011. Extracellular matrix degradation and remodeling in development and disease. *Cold Spring Harb Perspect Biol*, 3.
 - MARCINK, T. C., SIMONCIC, J. A., AN, B., KNAPINSKA, A. M., FULCHER, Y. G., AKKALADEVI, N., FIELDS, G. B. & VAN DOREN, S. R. 2019. MT1-MMP Binds Membranes by Opposite Tips of Its beta Propeller to Position It for Pericellular Proteolysis. *Structure*, 27, 281-292 e6.

- MARGIOTTA, A., PROGIDA, C., BAKKE, O. & BUCCI, C. 2017. [Rab7a regulates cell migration through Rac1 and vimentin](#). *Biochim Biophys Acta Mol Cell Res*, 1864, 367-381.
- MCINROY, L. & MAATTA, A. 2007. [Down-regulation of vimentin expression inhibits carcinoma cell migration and adhesion](#). *Biochem Biophys Res Commun*, 360, 109-14.
- MCMICHAEL, B. K., CHENEY, R. E. & LEE, B. S. 2010. [Myosin X regulates sealing zone patterning in osteoclasts through linkage of podosomes and microtubules](#). *J Biol Chem*, 285, 9506-9515.
- MENKO, A. S., BLEAKEN, B. M., LIBOWITZ, A. A., ZHANG, L., STEPP, M. A. & WALKER, J. L. 2014. [A central role for vimentin in regulating repair function during healing of the lens epithelium](#). *Mol Biol Cell*, 25, 776-90.
- MESSICA, Y., LASER-AZOGUI, A., VOLBERG, T., ELISHA, Y., LYSAKOVSKAIA, K., EILS, R., GLADILIN, E., GEIGER, B. & BECK, R. 2017. [The role of Vimentin in Regulating Cell Invasive Migration in Dense Cultures of Breast Carcinoma Cells](#). *Nano Lett*, 17, 6941-6948.
- MIIHKINEN, M., GRONLOH, M. L. B., POPOVIC, A., VIHINEN, H., JOKITALO, E., GOULT, B. T., IVASKA, J. & JACQUEMET, G. 2021. [Myosin-X and talin modulate integrin activity at filopodia tips](#). *Cell Rep*, 36, 109716.
- MOHAMMADI, H., ARORA, P. D., SIMMONS, C. A., JANMEY, P. A. & MCCULLOCH, C. A. 2015. [Inelastic behaviour of collagen networks in cell-matrix interactions and mechanosensation](#). *J R Soc Interface*, 12, 20141074.
- NCI, N. C. I. 2022. The Cancer Genome Atlas.
- NIETO, M. A. 2009. [Epithelial-Mesenchymal Transitions in development and disease: old views and new perspectives](#). *Int J Dev Biol*, 53, 1541-7.
- NIETO, M. A., HUANG, R. Y., JACKSON, R. A. & THIERY, J. P. 2016. [Emt: 2016](#). *Cell*, 166, 21-45.
- OSTROWSKA-PODHORODECKA, Z., DING, I., LEE, W., TANIC, J., ABBASI, S., ARORA, P. D., LIU, R. S., PATTESON, A. E., JANMEY, P. A. & MCCULLOCH, C. A. 2021. [Vimentin tunes cell migration on collagen by controlling beta1 integrin activation and clustering](#). *J Cell Sci*, 134.
- PALL, T., PINK, A., KASAK, L., TURKINA, M., ANDERSON, W., VALKNA, A. & KOGERMAN, P. 2011. [Soluble CD44 interacts with intermediate filament protein vimentin on endothelial cell surface](#). *PLoS One*, 6, e29305.
- PETRIE, R. J., KOO, H. & YAMADA, K. M. 2014. [Generation of compartmentalized pressure by a nuclear piston governs cell motility in a 3D matrix](#). *Science*, 345, 1062-5.
- PLANTARD, L., ARJONEN, A., LOCK, J. G., NURANI, G., IVASKA, J. & STROMBLAD, S. 2010. [PtdIns\(3,4,5\)P\(3\) is a regulator of myosin-X localization and filopodia formation](#). *J Cell Sci*, 123, 3525-34.
- RAWLA, P., SUNKARA, T. & BARSOUK, A. 2019. [Epidemiology of colorectal cancer: incidence, mortality, survival, and risk factors](#). *Prz Gastroenterol*, 14, 89-103.
- ROBERT, A., HOOKWAY, C. & GELFAND, V. I. 2016. [Intermediate filament dynamics: What we can see now and why it matters](#). *Bioessays*, 38, 232-43.
- ROBERT, A., ROSSOW, M. J., HOOKWAY, C., ADAM, S. A. & GELFAND, V. I. 2015. [Vimentin filament precursors exchange subunits in an ATP-dependent manner](#). *Proc Natl Acad Sci U S A*, 112, E3505-14.
- ROGOJANU, R., THALHAMMER, T., THIEM, U., HEINDL, A., MESTERI, I., SEEWALD, A., JAGER, W., SMOCHINA, C., ELLINGER, I. & BISES, G. 2015. [Quantitative Image Analysis of Epithelial and Stromal Area in Histological Sections of Colorectal Cancer: An Emerging Diagnostic Tool](#). *Biomed Res Int*, 2015, 569071.

- ROUT-PITT, N., FARROW, N., PARSONS, D. & DONNELLEY, M. 2018. [Epithelial mesenchymal transition \(EMT\): a universal process in lung diseases with implications for cystic fibrosis pathophysiology.](#) *Respir Res*, 19, 136.
- RUDOLPH, J., CRAWFORD, J. J., HOEFLICH, K. P. & CHERNOFF, J. 2013. [p21-activated kinase inhibitors.](#) *Enzymes*, 34 Pt. B, 157-80.
- SANGHVI-SHAH, R. & WEBER, G. F. 2017. [Intermediate Filaments at the Junction of Mechanotransduction, Migration, and Development.](#) *Front Cell Dev Biol*, 5, 81.
- SATELLI, A. & LI, S. 2011. [Vimentin in cancer and its potential as a molecular target for cancer therapy](#) *Cell Mol Life Sci*, 68, 3033-46.
- SHIBUE, T. & WEINBERG, R. A. 2017. [EMT, CSCs, and drug resistance: the mechanistic link and clinical implications](#) *Nat Rev Clin Oncol*, 14, 611-629.
- STROUHALOVA, K., PRECHOVA, M., GANDALOVICOVA, A., BRABEK, J., GREGOR, M. & ROSEL, D. 2020. [Vimentin Intermediate Filaments as Potential Target for Cancer Treatment](#) *Cancers (Basel)*, 12.
- SUN, Y. Y., YANG, Y. F. & KELLER, K. E. 2019. [Myosin-X Silencing in the Trabecular Meshwork Suggests a Role for Tunneling Nanotubes in Outflow Regulation.](#) *Invest Ophthalmol Vis Sci*, 60, 843-851.
- TERRIAC, E., COCEANO, G., MAVAJIAN, Z., HAGEMAN, T. A., CHRIST, A. F., TESTA, I., LAUTENSCHLAGER, F. & GAD, A. K. 2017. [Vimentin Levels and Serine 71 Phosphorylation in the Control of Cell-Matrix Adhesions, Migration Speed, and Shape of Transformed Human Fibroblasts.](#) *Cells*, 6.
- THIERY, J. P., ACLOQUE, H., HUANG, R. Y. & NIETO, M. A. 2009. [Epithelial-mesenchymal transitions in development and disease.](#) *Cell*, 139, 871-90.
- TOIYAMA, Y., YASUDA, H., SAIGUSA, S., TANAKA, K., INOUE, Y., GOEL, A. & KUSUNOKI, M. 2013. [Increased expression of Slug and Vimentin as novel predictive biomarkers for lymph node metastasis and poor prognosis in colorectal cancer.](#) *Carcinogenesis*, 34, 2548-57.
- TOKUO, H., MABUCHI, K. & IKEBE, M. 2007. [The motor activity of myosin-X promotes actin fiber convergence at the cell periphery to initiate filopodia formation.](#) *J Cell Biol*, 179, 229-38.
- TSURUTA, D. & JONES, J. C. 2003. [The vimentin cytoskeleton regulates focal contact size and adhesion of endothelial cells subjected to shear stress.](#) *J Cell Sci*, 116, 4977-84.
- WATANABE, A., HOSHINO, D., KOSHIKAWA, N., SEIKI, M., SUZUKI, T. & ICHIKAWA, K. 2013. [Critical role of transient activity of MT1-MMP for ECM degradation in invadopodia.](#) *PLoS Comput Biol*, 9, e1003086.
- WATANABE, T. M., TOKUO, H., GONDA, K., HIGUCHI, H. & IKEBE, M. 2010. [Myosin-X induces filopodia by multiple elongation mechanism.](#) *J Biol Chem*, 285, 19605-14.
- WOLF, K., WU, Y. I., LIU, Y., GEIGER, J., TAM, E., OVERALL, C., STACK, M. S. & FRIEDL, P. 2007. [Multi-step pericellular proteolysis controls the transition from individual to collective cancer cell invasion.](#) *Nat Cell Biol*, 9, 893-904.
- YU, H., MOUW, J. K. & WEAVER, V. M. 2011. [Forcing form and function: biomechanical regulation of tumor evolution](#) *Trends Cell Biol*, 21, 47-56.
- YUDA, A. & MCCULLOCH, C. A. 2018. [A Screening System for Evaluating Cell Extension Formation, Collagen Compaction, and Degradation in Drug Discovery.](#) *SLAS Discov*, 23, 132-143.
- ZEINDL-EBERHART, E., BRANDL, L., LIEBMANN, S., ORMANN, S., SCHEEL, S. K., BRABLETZ, T., KIRCHNER,

- T. & JUNG, A. 2014. Epithelial-mesenchymal transition induces endoplasmic- reticulum-stress response in human colorectal tumor cells. *PLoS One*, 9, e87386.
- ZHANG, H., BERG, J. S., LI, Z., WANG, Y., LANG, P., SOUSA, A. D., BHASKAR, A., CHENEY, R. E. & STROMBLAD, S. 2004. Myosin-X provides a motor-based link between integrins and the cytoskeleton *Nat Cell Biol*, 6, 523-31.
 - ZHANG, H., QI, M., LI, S., QI, T., MEI, H., HUANG, K., ZHENG, L. & TONG, Q. 2012 microRNA-9 targets matrix metalloproteinase 14 to inhibit invasion, metastasis, and angiogenesis of neuroblastoma cells. *Mol Cancer Ther*, 11, 1454-66.

Figure Legends

Fig. 1. Vimentin colocalize with myosin 10 in CRC

Representative images of colon tissue staining with DAPI (blue), Vim (red), Myo10 (green), and their colocalization (yellow) areas in (A) normal (control) tissue, and (B) progressing adenocarcinoma (tumor). Images were obtained by Zeiss Axio Scan.Z1 microscope, objective 20x. (C and D) Quantification of Pearson colocalization for Vim and Myo10 in normal and tumor estimated for (C) epithelium and (D) stoma region. Mean fluorescence intensity (MFI) for (E) Myo10 and (D) Vim was detected separately in epithelium and stroma regions of normal and tumor tissue specimens (n=26 for normal and tumor samples, Unpair t-test significance **p<0.01).

Fig. 2 Vim expression affects Myo10 trafficking towards the tips of cell extensions.

(A) Whole-cell lysates of mEF (WT, KO, and ULF) and SW480 cells cultured on Col (1 mg/ml) for 3, 6 and 24h. Cells were immunoblotted for Myo10, Vim and β -actin with appropriate antibodies. (B) Representative confocal images of mEF WT and Vim KO cells cultured on Col. Cells were triple stained for Vim (red), Myo10 (magenta) and actin (green). (C) Quantification of the number of cell protrusions decorated with Myo10 at the end of cell extension after 3, 6 and 24h growth. Images were quantified with ImageJ (n=3; 35 cells per group). Data are shown as a mean \pm S.E.M. 2way ANOVA significance *p<0.05, ***p<0.001, ****p<0.0001 compared with WT. (D) Vim and Myo10 immunoprecipitations (IP) in mEF WT cells. Left panel: IP of Myo10 was immunoblotted for Vim. Right panel: IP of Vim was immunoblotted for Myo10. An irrelevant antibody (IgG) was used as the immunoprecipitation control. Bottom row shows input Myo10, and Vim immunoblot. Actin was used as a loading control. (E) Hi-resolution STED images of mEF WT on Col and immunostained for Myo10 (red) and Vim (green). Scale bar 10 μ m, 2 μ m and 1 μ m. (F) Pearson coefficients obtained by quantification of the STED images of mEF WT (black), KO (red) and ULF (green) cells plated on Col with the Fiji JACoP plug-in. Scale bar, 2 μ m. All data are reported as a mean \pm S.E.M, n=3. (G). Representative donor and acceptor pre- and postbleach images are shown for AP-FRET. Arrows highlight areas of interaction. De-quenched signal from the donor (GFP) was seen after photobleaching the acceptor demonstrating interaction between Vim and Myo10. (H) FRET efficiency (E%) for Vim-Myo10 interaction in mEF WT (black) and mEF ULF (green) cells in (n=40; a mean \pm S.E.M, (p<0.001)). (I) Representative confocal images of mEF WT and SW480 cells before and after treatment with IPA3 (5 μ M) stained for Myo10 (magenta), Vim (green), actin (yellow) and nucleus (blue). Scale bar, 15 μ m. Arrows shows Myo10 particles displacement from the cell extension tip (top image) to the cell body (bottom image). (J) Quantification of the mean size of Myo10 particles in

vehicle and IPA3 treated cells. mEF WT (black), KO (red), ULF (green) and SW480 (blue). Empty bars indicate samples after IPA3 treatment cells. Images were quantified with ImageJ (n=3, 30 cells per group). (K) Myo10 and Vim IP in mEFs (WT, KO, ULF) and SW480 cells before and after treatment with IPA3 (5 μ M). Upper panel: IP of Vim was immunoblotted for Myo10. Below: IP of Myo10 was immunoblotted for Vim. An irrelevant antibody (IgG) was used as control. Lower panel shows input Myo10, Vim and actin, which was used as a loading control. (L and M) Quantification of immunoprecipitated Myo10 (L) and Vim (M) from WB in comparison to protein input. MEF WT (black), KO (red), ULF (green) and SW480 (blue). Empty bars represent data obtained from IPA3 treatment cells (n=3 independent experiments). Data are shown as a mean \pm S.E.M. 2way ANOVA significance *p<0.05, **p<0.01, compared with WT.

Fig. 3. Vimentin regulates myosin10 substitution dynamics.

(A) Representative live cell images for FRAP in cells transfected with GFP-Myo10. Images before bleaching (Pre-bleach), after bleach (Bleach), at intermediate recovery point (Half-recovery), and at the end of record fluorescent recovery (End-recovery); regions of interest (ROIs: 1 μ m² area indicated with arrow). Fluorescence in ROIs was measured before bleaching and for 150 s after bleaching with argon laser at 488 nm. Cells were cultured on fibrillar Col-coated surface for 3 h. (B) Typical normalized FRAP curves are displayed in mEF WT (black), KO (red), ULF (green), Vim rescue (magenta), SW480 (blue) and SW480 Vim KD (light blue). (C) FRAP mobile fractions, and (D) The FRAP-half-life recovery. All FRAP images were quantified with ImageJ (n=3, 15 cells per group). (E) Estimation of Myo10 velocity in protruding cells mEF WT (black), KO (red), ULF (green) and Vim rescue (magenta). Data are shown as a mean \pm S.E.M. One-way ANOVA significance *p<0.05, **p<0.01, ***p<0.001, ****p<0.0001 compared with WT.

Fig. 4. Loss of filamentous vimentin reduces traction forces and collagen remodeling.

(A) Representative images of cells cultured on fibrillar Col gels for 5 h to evaluate and quantify Col fiber alignment (B), and compaction (C) for mEF WT (black), KO (red), ULF (green), Vim rescue (magenta), SW480 (blue) and SW480 Vim KD (light blue). Scale bar, 15 μ m. (D) Images of cells cultured on Col gels for mEF WT and mEF KO before and after treatment with Myo10 siRNA. Cells were stained with rhodamine-phalloidin, and the yellow line shows the cell outline. (E) Estimation of Col fibers alignment and (F) and compaction for mEF WT (black), mEF WT Myo10 KD (gray), KO (red), and mEF KO Myo10 KD (light red). Scale bar, 15 μ m. (G) Col tractional remodeling was quantified by analyzing position changes of marker beads embedded in Col gels over a 5 h sampling period. (H) Bead displacement was used to calculate mean cell-induced deformations by particle image velocimetry, displayed as vectors with a color-coded magnitude as indicated in H. (I) Images of mEF WT, mEF KO and mEF ULF cells cultured for 6 h into Col gels (1 mg/ml) and stained for 3/4 collagen. The yellow line shows the cell outline; scale bar, 10 μ m. (J) Quantification of Col degradation by mEF WT (black), KO (red) and ULF (green), cells embedded in a 3D type I collagen matrix using anti-Collagen Type 1 (3/4 fragment) antibody. Data are reported as mean \pm S.E.M, n=3 (30 cells per group). One-way ANOVA significance *p<0.05, **p<0.01, ***p<0.001, ****p<0.0001 compared with WT. Scale bar, 20 μ m.

Fig. 5. Vimentin expression controls collagen fibers degradation via MT1-MMP regulation.(A) MT1-MMP activity (green) in cells cultured on Col gels for 6 h; actin indicates cell shape (red); scale bar, 20 μ m. (B) Fluorescence intensity of

mEF WT (black), KO (red) and ULF (green), cells stained for MT-MMP. One-way ANOVA significance ** $p < 0.01$, **** $p < 0.0001$ compared with WT. (C) Immunoblot of Myo10 KD efficiency. Cells were treated with scrambled siRNA (control) or FlexiTube Myo10_5 and Myo10_6 siRNA. (D) Representative live cell images for FRAP measurements; cells were transfected with GFP-MT1-MMP. Fluorescence in ROIs was measured before bleaching and for 150 s after bleaching with argon laser at 488 nm. MEF WT and Vim KO cells were cultured on fibrillar Col for 3 h. (E) Typical normalized FRAP curves for each condition are displayed in mEF WT (black) and KO (red), empty symbols indicate Myo10 KD cells. (F) The FRAP-half-life recovery, and (G) mobile fractions; images were quantified with ImageJ ($n=3$; 22 cells per group). (H) Quantification of the relative abundance of membrane-associated MT1-MMP by flow cytometry. MEF WT (black), KO (red) and ULF (green). Data are reported as a mean \pm S.E.M; $n=3$, 50000 cells. * $p < 0.05$, ** $p < 0.01$. (I) WB of Col-bead associated focal adhesion and whole-cell lysate (input) proteins for mEF WT, KO and ULF cells, stained for Myo10, MT1-MMP, Vim and β -actin (as a loading control). (J) Activated fraction of MT1-MMP in detected in mEF WT (black), KO (red) and ULF (green). Data are reported as a mean \pm S.E.M; $n=3$. * $p < 0.05$.

Fig. 6. Model of the vimentin-dependent collagen remodeling regulation by controlling the assembly of Myo10.

After the initial cell extension formation, Vim organizes Myo10 trafficking at the tip of cell extension, where Myo10 is aggregated, which strengthens the cell-ECM attachment. This, in turn, accelerates collagen alignment and its digestion by MT1-MMP presented at the surface of the cell membrane. Vim is involved in MT1-MMP secretion, stimulated proteolysis, and reorganization of the Col fibers, which helps to promote cell motility. Diagram was created with BioRender.com.

Figure_1

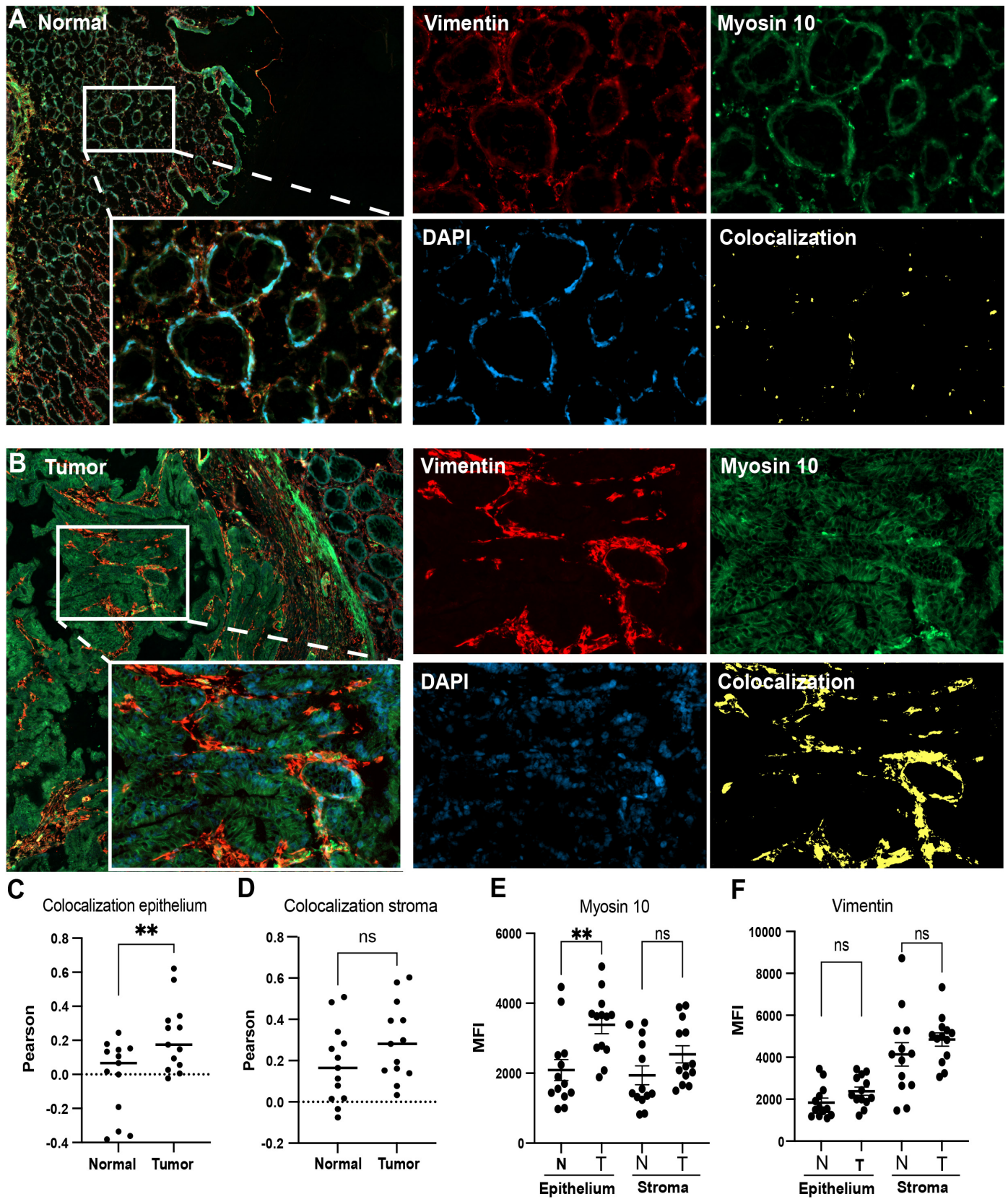


Figure_2

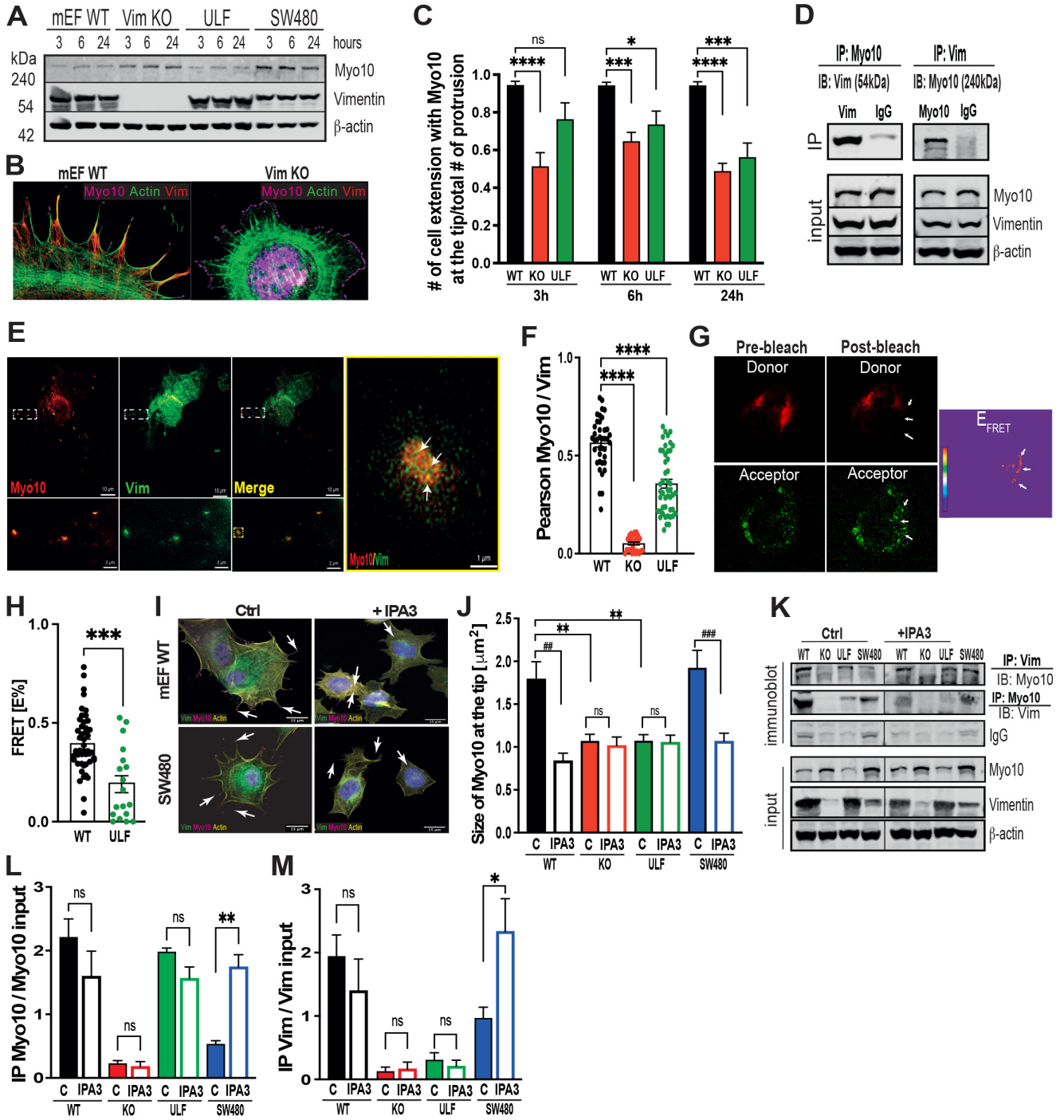


Figure_3

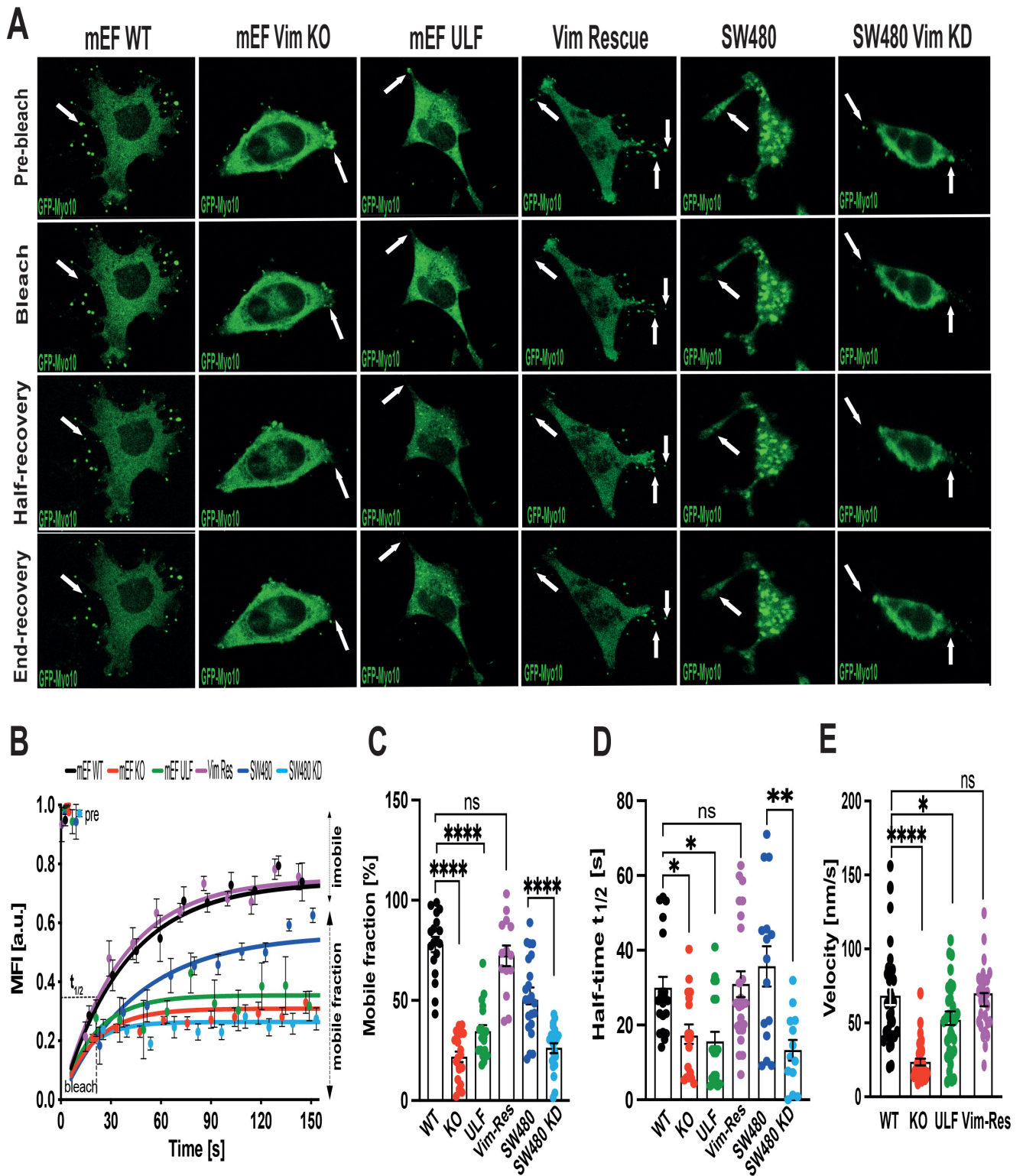


Figure_4

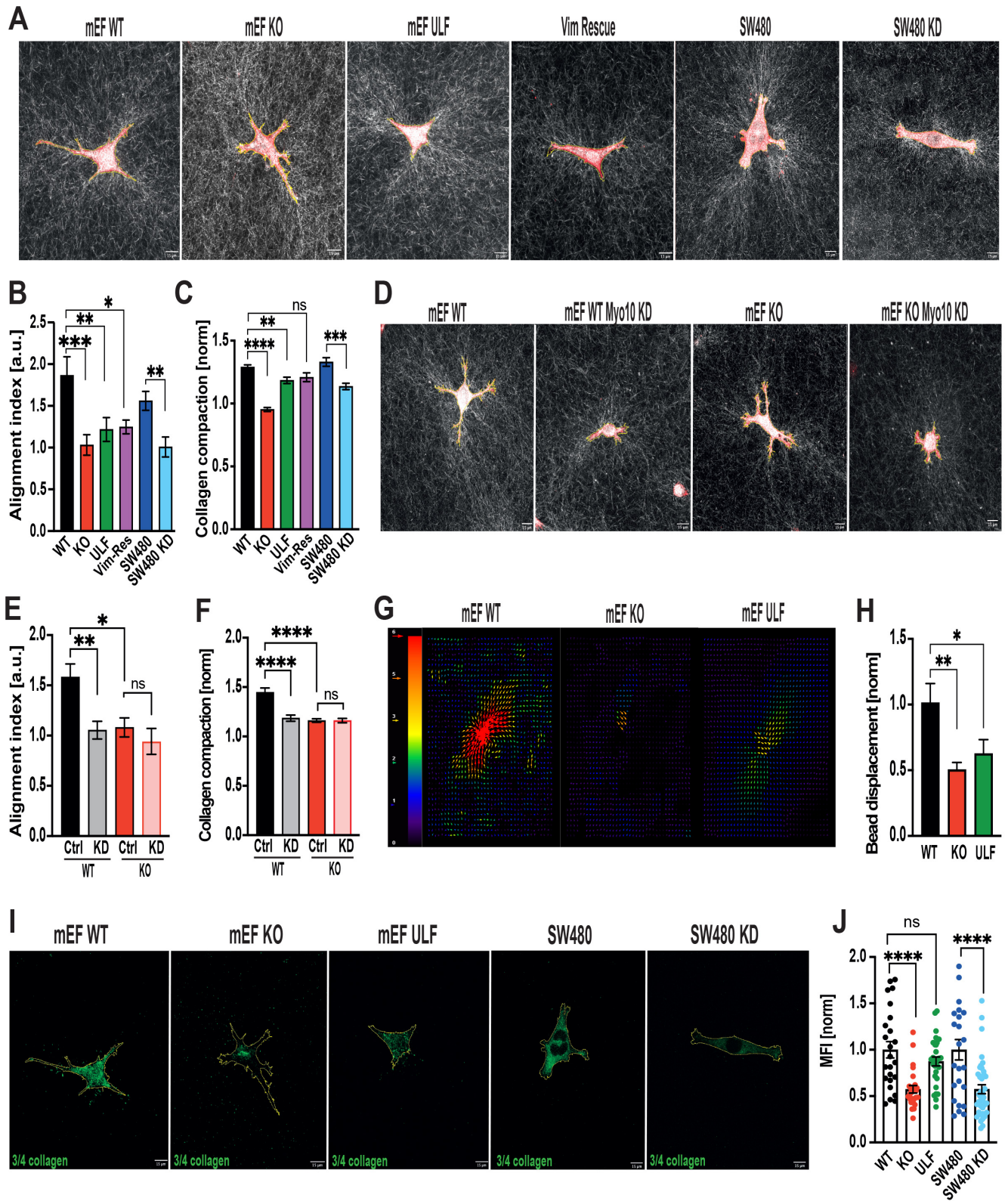


Figure_5

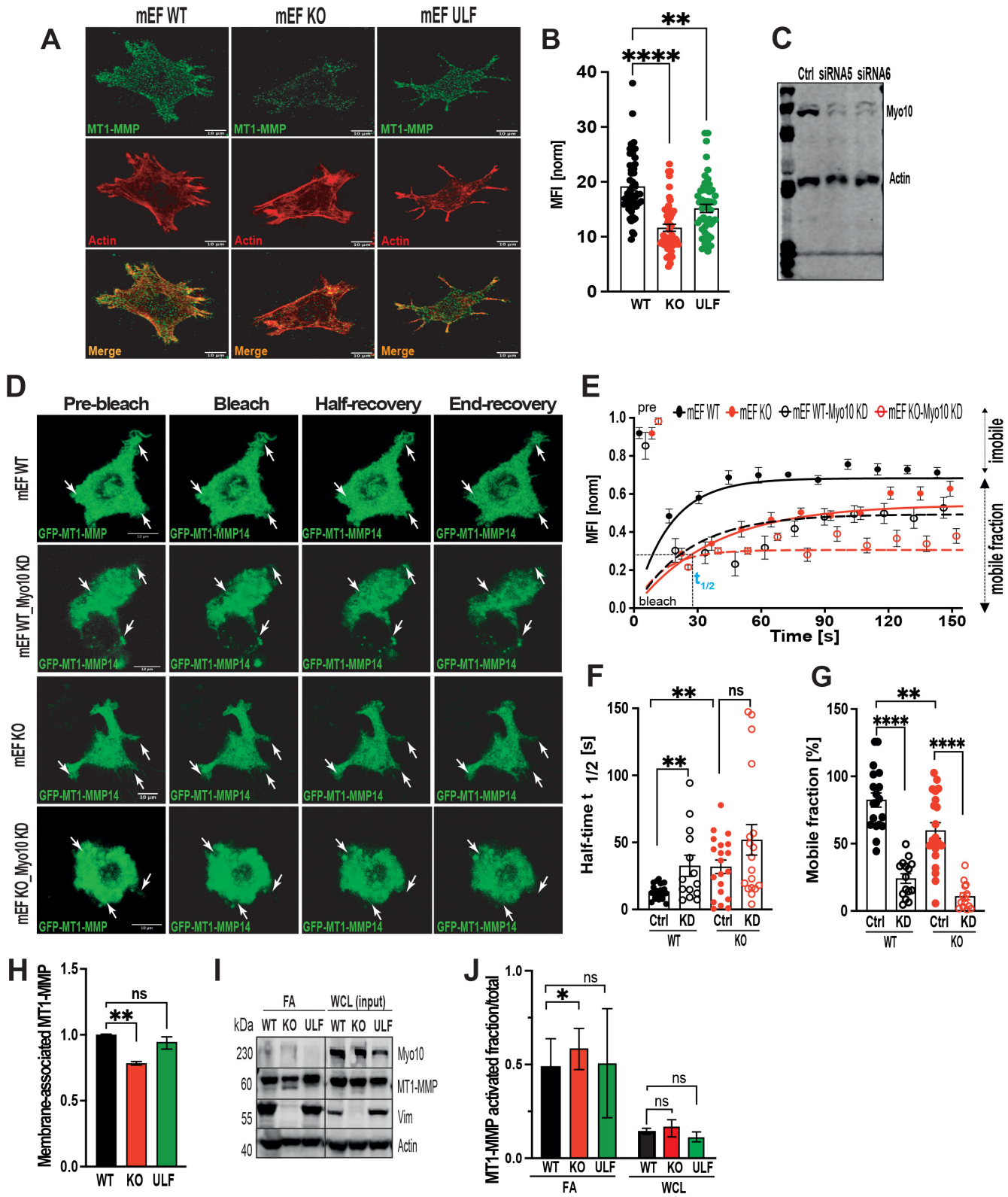


Figure_6

